Journal of Solid State Chemistry 183 (2010) 1477–1483

Contents lists available at ScienceDirect

Journal of Solid State Chemistry

journal homepage: www.elsevier.com/locate/jssc

Effects of rare-earth substitution in the oxyarsenides *RE*FeAsO (*RE*=Ce, Pr, Nd, Sm, Gd) and CeNiAsO by X-ray photoelectron and absorption spectroscopy

Peter E.R. Blanchard, Ronald G. Cavell, Arthur Mar *

Department of Chemistry, University of Alberta, Edmonton, Alberta, Canada T6G 2G2

ARTICLE INFO

Article history:
Received 13 January 2010
Received in revised form
7 April 2010
Accepted 9 April 2010
Available online 13 April 2010

Keywords:
XPS
XANES
Oxyarsenides

ABSTRACT

X-ray photoelectron spectroscopy (XPS) and X-ray absorption near-edge spectroscopy (XANES) have been applied to examine the electronic structure of the rare-earth transition-metal oxyarsenides *RE*FeAsO (*RE*=Ce, Pr, Nd, Sm, Gd) and CeNiAsO. Within the metal–arsenic layer [*M*As], the bonding character is predominantly covalent and the As atoms are anionic, as implied by the small energy shifts in the *M* 2*p* and As 3*d* XPS spectra. Within the rare-earth–oxygen layer [*RE*O], the bonding character is predominantly ionic, as implied by the similarity of the O 1*s* binding energies to those in highly ionic oxides. Substitution with a smaller *RE* element increases the O 1*s* binding energy, a result of an enhanced Madelung potential. The Ce 3*d* XPS and Ce L_3-edge XANES spectra have lineshapes and energies that confirm the presence of trivalent cerium in CeFeAsO and CeNiAsO. A population analysis of the valence band spectrum of CeNiAsO supports the formal charge assignment $[Ce^{3+}O^{2-}][Ni^{2+}As^{3-}]$.

1. Introduction

The recent discovery of a new family of superconductors derived from the rare-earth transition-metal oxyarsenides *REM*AsO has provoked frequent comparisons to the cuprate superconductors [1]. In the tetragonal ZrCuSiAs-type crystal structure of the oxyarsenides [2], in which the [*RE*O] and [*M*As] layers are stacked in an alternating fashion, with the O and *M* atoms tetrahedrally coordinated by *RE* and As atoms, respectively (Fig. 1), the supposition is that the [*RE*O] layer acts as a charge reservoir, similar to the cuprates [1]. The parent oxyarsenides themselves are unextraordinary; for example, LaNiAsO is the only quaternary oxyarsenide known so far that behaves as a superconductor (T_c=2.75 K) [3]. Doping the oxygen site with a small amount of fluorine leads to higher T_c values, but the effect of *RE* substitution is not so obvious (e.g., $LaFeAsO_{1-x}F_x$, 43 K [1]; $CeFeAsO_{1-x}F_x$, 41 K [4]; $PrFeAsO_{1-x}F_x$, 52 K [5]; $NdFeAsO_{1-x}F_x$, 51 K [6]; $SmFeAsO_{1-x}F_x$, 54.6 K [7]; $GdFeAsO_{1-x}F_x$, 36 K [8]). Experimental investigations of the electronic structure are important for further understanding and development of these materials.

We have applied X-ray photoelectron spectroscopy (XPS) and X-ray absorption near-edge spectroscopy (XANES) to probe the electronic structure of various binary and ternary pnictides [9–12], which are more difficult to analyze because of their reduced ionic character compared to oxides and halides. Simple electron counting for the oxyarsenides suggests the formulation $[RE^{3+}O^{2-}][M^{2+}As^{3-}]$, but this is an approximation that neglects the different degrees of ionic and covalent character within the separate layers. For example, as we have demonstrated for La*M*AsO (*M*=Fe, Co, Ni), an unsophisticated interpretation of binding energy shifts alone leads to apparent charges of M^{1+} and As^{1-}, but an analysis of the valence band spectra in which components are fitted to individual atomic states can recover the expected formulation $[La^{3+}O^{2-}][M^{2+}As^{3-}]$ [11]. Other XPS and XANES studies have concentrated on the doped iron-containing representatives $REFeAsO_{1-x}F_x$, some of the major conclusions being that delocalization of the Fe *d*-electrons occurs and that fluorine-doping introduces additional charge into the [FeAs] layer without directly altering the density of states near the Fermi level [13–19].

In this paper, we focus attention on the [*RE*O] layer to evaluate the effects of *RE* substitution in the iron-containing series *RE*FeAsO (*RE*=Ce, Pr, Nd, Sm, Gd) by means of high-resolution core-line (*RE* 3*d*, Fe 2*p*, As 3*d*, and O 1*s*) and valence band XPS spectra. The XPS (Ce 3*d*, Ni 2*p*, As 3d, O 1*s*) and XANES (Ce L_3-edge; Ni *L*- and *M*-edges) spectra for the nickel-containing compound CeNiAsO were also measured to allow a comparison to the previously studied compound LaNiAsO [11].

2. Experimental

2.1. Synthesis and X-ray diffraction

All reagents, obtained from Alfa-Aesar, Cerac, or Hefa with purities generally better than 99.5%, were handled in an Ar-filled

* Corresponding author. Fax: +1 780 492 8231.
E-mail address: arthur.mar@ualberta.ca (A. Mar).

0022-4596/$ - see front matter © 2010 Elsevier Inc. All rights reserved.
doi:10.1016/j.jssc.2010.04.010

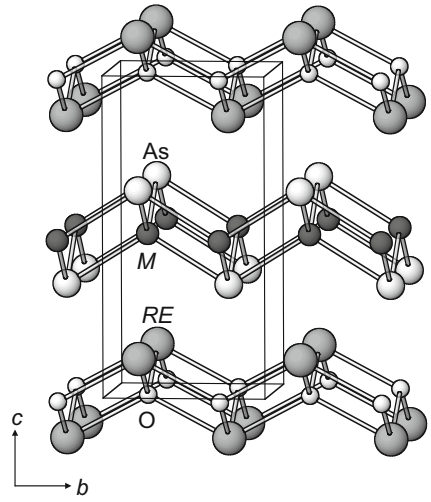

Fig. 1. Crystal structure of *REMA*sO in terms of alternating [*REO*] and [*MA*s] layers stacked along the *c*-direction.

glove box. Binary arsenides *RE*As (*RE*=Ce, Pr, Nd, Sm, Gd) were prepared from stoichiometric reactions of elemental *RE* and As at 1050 °C for 2 days. Binary oxides CeO_2, RE_2O_3 (*RE*=Pr, Nd, Sm, Gd), Fe_2O_3, and NiO were dehydrated by heating at 900 °C for 2 days. The quaternary oxyarsenides *RE*FeAsO and CeNiAsO were prepared from stoichiometric mixtures of the appropriate starting materials: CeFeAsO (from CeAs, CeO_2, FeAs, and Fe); PrFeAsO (from PrAs, Fe_2O_3, and Fe); NdFeAsO (from NdAs, Nd_2O_3, FeAs, and Fe_2As); SmFeAsO (from SmAs, Fe_2O_3, and Fe); GdFeAsO (from GdAs, Gd_2O_3, FeAs, and Fe); CeNiAsO (from CeAs and NiO). The mixtures were finely ground and loaded into alumina crucibles placed within fused-silica tubes, which were evacuated, sealed, and heated at 1250 °C for 3 days. The products were judged to be single-phase from their powder X-ray diffraction (XRD) patterns measured on an Inel powder diffractometer (Fig. S1 in Supplementary Data). Although the compound CeNiAsO has been reported [20], no structural information has been available. With initial positions taken from the isotypic oxyarsenides, the crystal structure of CeNiAsO was refined with the full-profile Rieteld method by using the program LHPM-Rietica [21]. The results are summarized in Table 1 and the fit to the powder XRD pattern is shown in Fig. 2.

2.2. XPS analysis

XPS spectra for all compounds prepared were measured on a Kratos AXIS 165 spectrometer equipped with a monochromatic Al*K*α X-ray source (14 mA, 15 kV) and a hybrid lens with a spot size of $700 \times 400\,\mu m^2$. The samples are air-stable but to minimize exposure to air, they were handled in an Ar-filled glove box where they were finely ground, pressed into In foil, mounted on a Cu sample holder, and placed in a sealed container for transfer to the analysis chamber of the spectrometer. The pressure inside the XPS instrument was maintained between 10^{-7} and 10^{-9} Pa. Samples were sputter-cleaned with an Ar^+ ion beam (4 kV, 10 mA) until core-line peaks associated with surface oxides were no longer observed in the XPS spectra. A small shoulder in the As 3*d* XPS spectra indicated that a slight reduction of As occurred; however, the binding energies (BE) in these and other spectra were, within standard uncertainties, the same before and after the sputtering procedure (Table S1 and Fig. S3 in Supplementary Data).

Survey spectra, collected with a BE range of 0–1100 eV, a pass energy of 160 eV, a step size of 0.7 eV, and a sweep time of 180 s, confirmed the expected chemical compositions (*RE*:*M*:As:O=1:1:1:1) for the oxyarsenides. High-resolution core-line spectra were collected with an energy envelope of appropriate range (Ce 3*d*, 60 eV; *M* 2*p*, 50 eV; As 3*d* and O 1*s*, 20 eV), a pass energy of 20 eV, a step size of 0.05 eV, and a sweep time of 180 s. Although no charge correction was required because the samples are good conductors, the spectra were calibrated to the C 1*s* line at 284.8 eV arising from adventitious carbon. All spectra were analyzed by using the CasaXPS software

Table 1
Crystallographic data for CeNiAsO.

Rietveld refinement results	
Formula	CeNiAsO
Formula mass (amu)	289.72
Space group	*P*4/*nmm* (No. 129)
a (Å)	4.0752(2)
c (Å)	8.1134(4)
V (Å^3)	134.74(1)
Z	2
ρ_{calcd} (g cm^{-3})	7.139
Radiation	Cu*K*α_1, λ=1.54056 Å
2θ range (deg.)	20.00–100.00
No. of data points	2759
No. of reflections	59
No. of variables	26
Residuals[a]	R_B=0.027; R_p=0.039; R_{wp}=0.054
GOF	3.89
Positional and displacement parameters	
Ce at 2*c* (1/4, 1/4, *z*)	
z	0.1481(4)
B_{iso} (Å^2)	0.28(6)
Ni at 2*b* (3/4, 1/4, 1/2)	
B_{iso} (Å^2)	1.2(2)
As at 2*c* (1/4, 1/4, *z*)	
z	0.6479(8)
B_{iso} (Å^2)	1.4(1)
O at 2*a* (3/4, 1/4, 0)	
B_{iso} (Å^2)	3.2(9)
Interatomic distances (Å)	
Ce–O (× 4)	2.365(2)
Ce–As (× 4)	3.323(5)
Ce–Ni (× 4)	3.508(3)
Ni–As (× 4)	2.365(3)
Ni–Ni (× 4)	2.8816(1)

[a] $R_B = \sum |I_o - I_c| / \sum I_o$; $R_p = \sum |y_o - y_c| / \sum y_o$; $R_{wp} = [\sum [w(y_o - y_c)] / \sum w y_o^2]^{1/2}$.

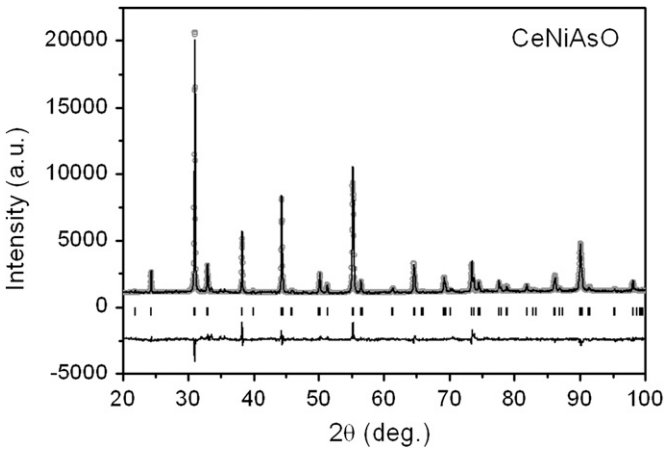

Fig. 2. Rietveld refinement results for CeNiAsO. The observed profile is indicated by circles and the calculated profile by the solid line. Bragg peak positions are located by the vertical tick marks. The difference plot is shown at the bottom.

Table 2
Core-line BEs (eV) for *RE*FeAsO (*RE*=La–Nd, Sm, Gd) and *RE*NiAsO (*RE*=La, Ce).

Sample	*RE* $3d_{5/2}$	Fe or Ni $2p_{3/2}$[a]	As $3d_{5/2}$	O 1*s*
LaFeAsO[b]	834.88	707.11	41.18	529.94
CeFeAsO	881.76	707.16	41.14	530.04
PrFeAsO	Not measured	707.09	41.14	530.09
NdFeAsO	Not measured	707.16	41.10	530.13
SmFeAsO	Not measured	707.10	41.13	530.17
GdFeAsO	Not measured	707.08	41.13	530.31
LaNiAsO [b]	834.92	Not measured	41.43	529.96
CeNiAsO	881.87	853.18	41.35	530.02

[a] For comparison, the $2p_{3/2}$ BEs are 707.0 eV for Fe metal and 852.7 eV for Ni metal [9,34].
[b] Values for LaFeAsO and LaNiAsO are taken from Ref. [11].

package [22]. The background arising from energy loss was removed by applying a Shirley-type function and the peaks were fitted to pseudo-Voigt (70% Gaussian and 30% Lorentzian) line profiles to take into account spectrometer and lifetime broadening effects. Table 2 lists all BE values expressed to two decimal places, with uncertainties estimated at better than ± 0.10 eV, as established by collecting multiple spectra (Table S1 in Supplementary Data).

2.3. XANES analysis

Ni *M*-edge XANES spectra for CeNiAsO were collected on the variable line spacing plane grating monochromator (PGM) beamline at the Canadian Light Source (CLS) in Saskatoon, Saskatchewan. Finely ground samples were mounted on carbon tape and inserted into the vacuum chamber via a load lock. Spectra were measured from ~20 eV below the edge to ~65 eV above the edge, with a step size of 0.1 eV through the edge. Spectra were collected in both total electron yield (TEY) and X-ray fluorescence yield (FLY) modes; however, because the Ni *M*-edge occurs at low energy and surface oxides become more apparent in the TEY spectra, only the FLY spectra are presented. The spectra were calibrated to Ni metal, with the maximum in the first derivative of its M_3-edge set to 66.2 eV [23].

RE L_3-edge XANES spectra for *RE*FeAsO (*RE*=La–Nd, Gd) and CeNiAsO were collected on the bending magnet beamline (20 BM) accessed through the Pacific Northwest Consortium/X-ray Operations and Research Collaborative Access Team (PNC/XOR-CAT), Sector 20 of the Advanced Photon Source (APS) at Argonne National Laboratory. Finely ground samples were sandwiched between Kapton tape and positioned at 45° to the X-ray beam. A silicon (111) double crystal monochromator provided a monochromatic photon flux of $\sim 10^{11}$ photons/s with a resolution of 1.4 eV at 10 keV and a beam size of approximately 1×4.5 mm. Spectra were measured in transmission mode with an ionization detector (filled with a 50:50 mixture of He and N_2 in the ionization chamber) and in fluorescence mode with a Canberra 13-element fluorescence detector. The step size was 0.1 eV through the absorption edge. Metal standards were placed behind the sample and measured concurrently in transmission mode. The *RE* L_3-edge spectra were calibrated to Cr (for *RE*=La–Nd) and Fe metal (for *RE*=Gd), with the maxima in the first derivatives of their *K*-edges set to 5989 and 7112 eV, respectively [23]. All XANES spectra were analyzed by using the Athena software program [23].

3. Results and discussion

3.1. [REO] layer

The general expectation is that the *RE* atoms within the [*REO*] layer of the oxyarsenides *REM*AsO are trivalent; however, there is a possibility that Ce can adopt other valence states. To this end, the Ce 3*d* XPS and L_3-edge XANES spectra for CeFeAsO and CeNiAsO were collected (Fig. 3). In general, the XPS BE shifts of rare-earth-containing compounds are relatively insensitive to changes in bonding character because of the increased nuclear screening provided by the 4*f* electrons [24]. However, the Ce 3*d* XPS lineshapes in CeFeAsO and CeNiAsO do resemble those in other trivalent cerium compounds (e.g., CeF_3 [24] $CeFe_4P_{12}$ [24], $CeFe_4Sb_{12}$ [25]), where characteristic satellite peaks are observed on the higher BE (by ~4 eV) side of each of the two core-line peaks representing the $3d_{5/2}$ and $3d_{3/2}$ spin-orbit-coupled final states (Fig. 3a). Relative to the core-line peaks, the intensity of these satellite peaks, which have been proposed to originate from various shake-up processes, is proportional to the degree of orbital overlap between the *RE* atom and its surrounding ligands (here, As and O atoms) [26–28]. The satellite peaks have the same intensity in CeFeAsO and CeNiAsO, implying that changing the metal has no effect on the [CeO] layer, but they are more intense than in LaFeAsO and LaNiAsO [11], a reflection of the greater orbital overlap provided by the $4f^1$ state in trivalent cerium. In the Ce L_3-edge XANES spectra for CeFeAsO and CeNiAsO (Fig. 3b), the occurrence of a single white line peak (labeled A), assigned as the dipole-allowed transition of a 2*p* electron into 6*s* or 5*d* states

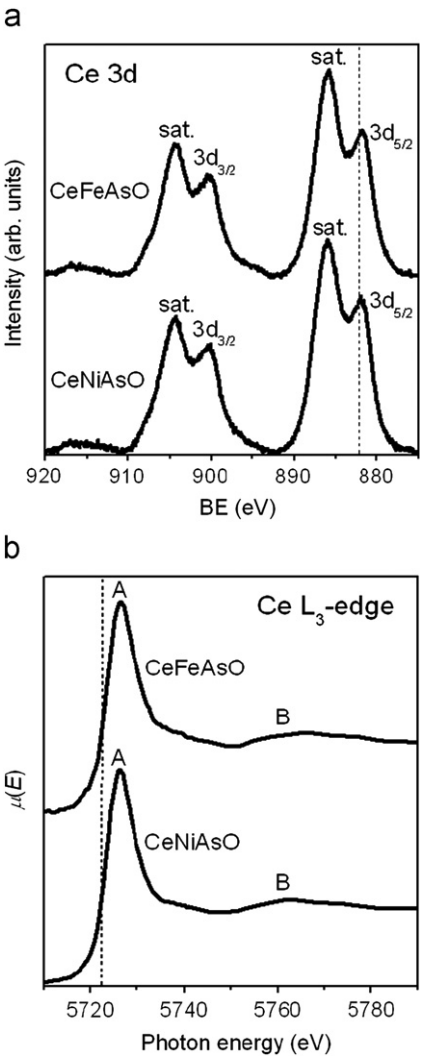

Fig. 3. (a) Ce 3*d* XPS and (b) Ce L_3-edge XANES spectra for CeFeAsO and CeNiAsO. The spectra are offset for clarity. The vertical dashed lines mark the Ce $3d_{5/2}$ BE in (a) and the absorption edge energy in (b).

($\Delta l = \pm 1$), indicates that only one valence state for Ce is present [29,30]. A second feature (labeled B) is interpreted as a continuum resonance associated with the shell of ligand atoms surrounding the absorbing atom [31]. The *RE* L_3-edge XANES spectra for other *RE*FeAsO members (*RE*=La, Pr, Nd, Gd) exhibit similar features (Fig. S2 in Supplementary Data). The confirmation of trivalent *RE* atoms has also been supported by previous *RE* *M*-edge XANES measurements on *RE*FeAsO (*RE*=La, Ce, Sm, Gd) [15].

Representative O 1*s* XPS spectra are selected for comparison (Fig. 4); spectra for the remaining compounds are also available (Fig. S3 in Supplementary Data). The O 1*s* BE values for these oxyarsenides range from 529.9 to 530.3 eV (Table 2). According to a classification scheme developed by Barr for correlating O 1*s* BE values to the degree of ionic character in metal-oxygen bonds (semicovalent oxides, 530.5–533.0 eV; normal ionic oxides, 529.6–530.4 eV; very ionic oxides, 528.0–529.5 eV) [32,33], the oxyarsenides fall in the category of normal ionic oxides. In contrast, binary rare-earth oxides tend to have BE values associated with very ionic bonding [32]. Thus, the *RE*–O bond becomes less ionic as we progress from the binary rare-earth oxides to the rare-earth oxyarsenides. Interestingly, the O 1*s* BE is virtually the same for differently substituted transition metals (cf. 530.04 eV in CeFeAsO vs. 530.02 eV in CeNiAsO) (Fig. 4a), consistent with the assertion above that the changes in the [*M*As] layer have little effect on the [*RE*O] layer. The O 1*s* BE

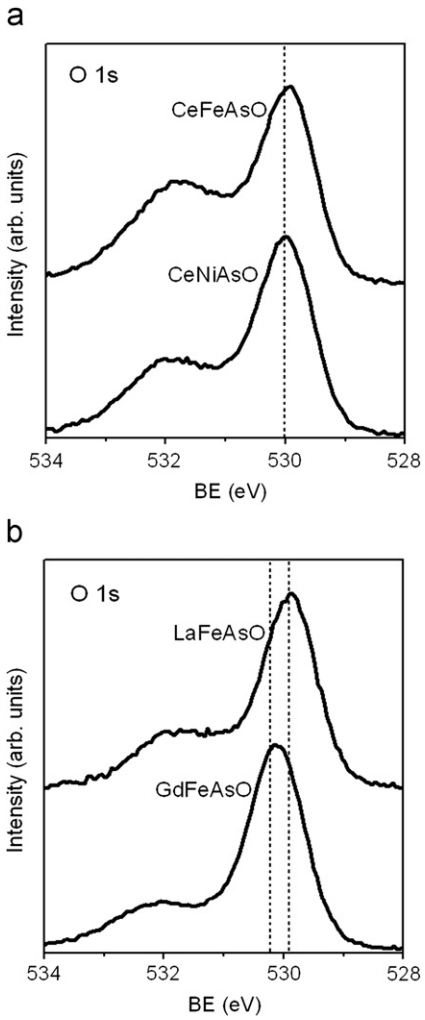

Fig. 4. O 1*s* XPS spectra for (a) CeFeAsO vs. CeNiAsO and (b) LaFeAsO vs. GdFeAsO. The spectra are offset for clarity. The vertical dashed lines mark the O 1*s* BE. The second peak at higher BE is attributed to a surface contaminant.

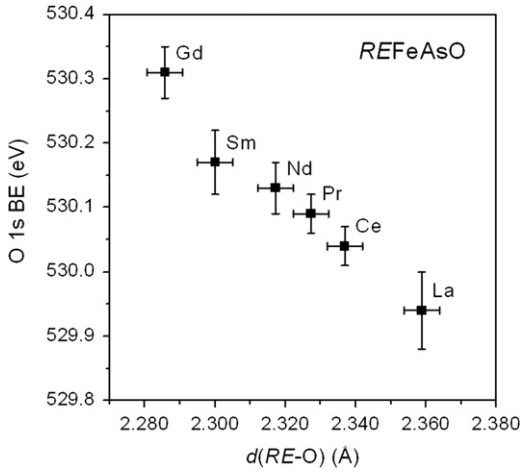

Fig. 5. Plot of O 1*s* BE vs. *RE*–O distance in *RE*FeAsO (*RE*=La–Nd, Sm, Gd).

increases perceptibly upon substitution with a smaller *RE* metal (cf. 529.94 eV in LaFeAsO vs. 530.31 eV in GdFeAsO) (Fig. 4b). One possible explanation might be that these BE shifts reflect changes in the degree of *RE*-to-O charge transfer, analogous to trends previously observed in the P $2p_{3/2}$ BE of metal phosphides as the electronegativity difference between component atoms is modified [9,34]. However, this explanation can be ruled out because the Allred-Rochow electronegativity difference between *RE* and O changes by less than 0.05 units upon substitution of La with Gd [35]. If ground state effects are assumed to be responsible for this trend, a more careful analysis requires consideration of the charge potential model, where the BE for an electron in an atom (E_i) is shifted relative to a reference energy (E_i^0) because of two factors [36]:

$$\Delta E_i = E_i - E_i^0 = k\Delta q_i + \Delta \sum_{j \neq i} q_j / r_{ij}. \quad (1)$$

The first term describes intraatomic effects, which scale with changes in charge on a given atom *i*, whereas the second term (a Madelung potential) describes interatomic effects, which scale with changes in the coordination environment defined by the surrounding atoms *j* with charges q_{ij} at some distance r_{ij}. Since intraatomic effects are minimal (given the similar electronegativities of *RE* atoms), we attribute the BE shifts to interatomic effects in which changes in r_{ij} are significant. As expected, when the *RE* component becomes smaller (from La to Gd) and the *RE*–O distances decrease, the O 1*s* BE shifts to higher energy (Fig. 5). Similar arguments have also been applied to account for the O 1*s* BE shifts in binary rare-earth oxides [37].

3.2. [*MA*s] layer

It is generally accepted that electronic conduction in the oxyarsenides *REMA*sO takes place primarily within the [*MA*s] layer. Evidence for this electronic delocalization can be sought through analysis of the *M* 2*p* XPS spectra (Fig. S3 in Supplementary Data). The most prominent feature, as seen in the representative spectra for CeFeAsO (Fig. 6a) and CeNiAsO (Fig. 6b), is the asymmetric lineshape exhibited by each of the $2p_{3/2}$ and $2p_{1/2}$ peaks, which are skewed towards higher BE. This asymmetry, which is indicative of the electronic delocalization found in metallic systems, arises when valence electrons, interacting with the core-hole, are scattered into the continuum of conduction states above the Fermi edge [38]. The electronic delocalization also causes the core electrons to experience significant nuclear screening such that the *M* 2*p* BEs are little shifted from those in

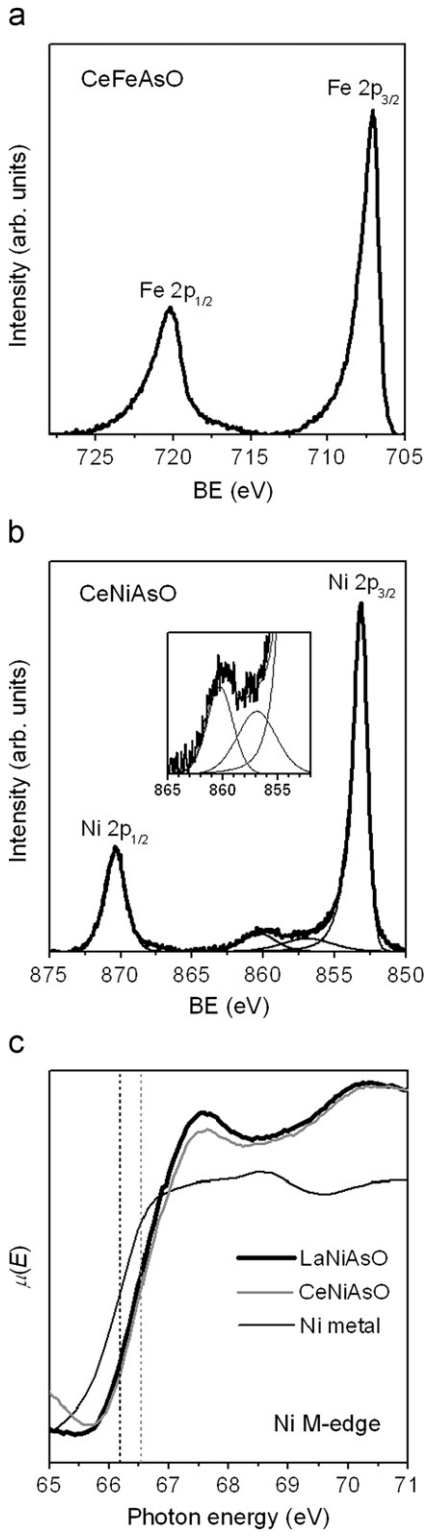

Fig. 6. (a) Fe 2*p* XPS spectrum for CeFeAsO and (b) Ni 2*p* XPS spectrum for CeNiAsO. The inset in (b) highlights the satellite feature. (c) Ni *M*-edge XANES spectra (FLY mode) for LaNiAsO, CeNiAsO, and Ni metal, with the absorption edges marked by vertical dashed lines.

the elemental metals. The shift in Fe 2*p* BE is barely discernible (cf. 707.1–707.2 eV in all *RE*FeAsO members vs. 707.0 in Fe metal [34]), whereas the shift in Ni 2*p* BE is somewhat more pronounced (cf. 853.2 eV in CeNiAsO vs. 852.7 eV in Ni metal [11]). In both cases, the slightly higher BE (relative to the elemental metal) is consistent with the presence of cationic *M* atoms, but in a delocalized system such as this, the BE is not necessarily a reliable indicator [9,34]. Note, however, that a satellite peak is found on the higher BE side of the Ni $2p_{3/2}$ core-line peak in the spectrum of CeNiAsO (Fig. 6b). We have previously interpreted this satellite peak [9,10,25], using either a two-core-hole or a plasmon loss model [39,40], to provide information about the Ni charge, with the satellite intensity being proportional to the number of valence states. Other recent studies suggest that both processes may be responsible for this satellite feature [41,42]. If a plasmon loss model is assumed, the satellite peak can be fitted to two components representing bulk plasmon (higher energy) and surface plasmon (lower energy) processes. The normalized satellite intensity ($I_{\text{satellite}}/I_{\text{core-line}}$) is lower in CeNiAsO (0.27) than in elemental Ni (0.38), indicating the presence of fewer valence states and thus positively charged Ni atoms. Further evidence for the cationic nature of the Ni atoms is provided by the higher absorption edge energies in the Ni *M*-edge XANES spectra for LaNiAsO and CeNiAsO (66.5 eV), compared to that for Ni metal (66.2 eV) (Fig. 6c). Spin-orbit-splitting into the M_3-edge ($3p_{3/2} \rightarrow 3d$) and M_2-edge ($3p_{1/2} \rightarrow 3d$) is evident in Ni metal, but not in LaNiAsO and CeNiAsO, likely because of peak broadening effects. (The higher-energy peak at 70.3 eV is attributed to a surface oxide.) The invariance of the Ni *M*-edge energy for LaNiAsO and CeNiAsO reaffirms the independence of the separate [*RE*O] and [*M*As] layers.

The As 3*d* XPS spectra for all members of the *RE*FeAsO series are similar (Fig. S3 in Supplementary Data). The spectra were fitted to two peaks corresponding to the $3d_{5/2}$ and $3d_{3/2}$ spin-orbit-coupled final states with a FWHM of 1.2–1.3 eV in an intensity ratio of 3:2. There is little difference in $3d_{5/2}$ BE values (41.1–41.2 eV), as expected because *RE* substitution has little effect on the [*M*As] layer. These BE values are lower than in elemental As (41.7(2) eV) [43,44], consistent with the presence of anionic As atoms, but the small shift reflects considerable covalency in the *M*–As bonds. Substitution of the *M* atoms, which are directly bonded to the As atoms, does lead to observable shifts in the As $3d_{5/2}$ BEs. Thus, for example, the As $3d_{5/2}$ BE is further lowered in CeFeAsO (41.1 eV) than in CeNiAsO (41.4 eV) relative to elemental As (Fig. 7); the greater electronegativity difference between Fe and As leads to a more pronounced metal-to-As

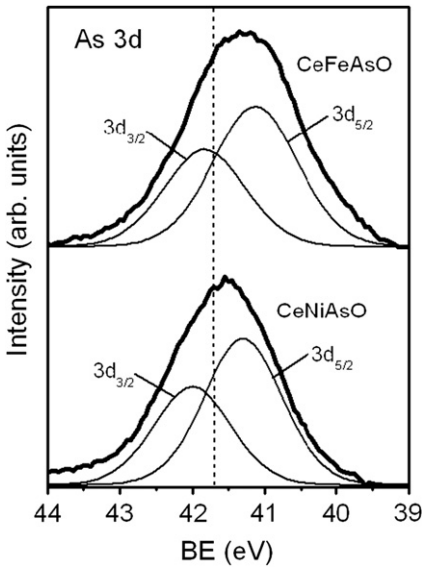

Fig. 7. As 3*d* XPS spectra for CeFeAsO and CeNiAsO, fitted with $3d_{5/2}$ and $3d_{3/2}$ component peaks. The vertical dashed line at 41.7 eV marks the $3d_{5/2}$ BE for elemental As.

charge transfer and more negatively charged As atoms in CeFeAsO.

3.3. Valence band spectrum of CeNiAsO

The XPS and XANES spectra presented above confirm the expectations of largely ionic character in the [*RE*O] layer and largely covalent character in the [*M*As] layer. The discrepancy with the idealized formulation $[RE^{3+}O^{2-}][M^{2+}As^{3-}]$ arises because the charge transfer within the [*M*As] layer is not as extreme as implied by these charges. Indeed, if such BE correlations are taken at face value, the As $3d_{5/2}$ BE in these oxyarsenides corresponds to a charge closer to 1− than 3− [43]. One way to recover the chemically valuable concept of valence state is to interpret the experimental valence band spectra through an electron population analysis, as we have applied to other compounds, including the La*M*AsO (*M*=Fe, Co, Ni) series [11,12,24,25,34,44]. In this procedure, an experimental valence band spectrum is compared to a calculated density of states, whose separate atomic projections can be used as a guide to assign individual component peaks. Several band structure calculations, at varying degrees of rigour, have been performed for these oxyarsenides *REM*AsO [11,45–51]. Here, we are interested in fitting the spectrum of CeNiAsO, and in particular, to determine if the 4*f* states in trivalent cerium can be detected.

The XPS valence band spectrum for CeNiAsO is shown in Fig. 8a. By comparison to calculated band structures, in particular that of LaNiAsO [11], the spectrum can be fitted to Ni 3*d* states at low BE, As 4*p*/O 2*p* states at intermediate BE, and As 4*s* states at high BE, with substantial mixing of the first two sets. In agreement with predictions that the Ce 4*f* states should lie near the Fermi edge [47], the valence band spectrum of CeNiAsO exhibits higher intensity at 1–2 eV when it is overlapped with that of LaNiAsO (Fig. 8b). These Ce 4*f* states are represented by peak 1. The Ni 3*d* states are split by a tetrahedral crystal field into t_2 ($3d_{5/2}$ as peak 2) and *e* sets ($3d_{5/2}$ and $3d_{3/2}$ as peaks 3 and 4, in a fixed intensity ratio of 3:2 and with somewhat greater FWHM because of metal-metal bonding interactions involving the $3d_{x^2-y^2}$ orbitals) [50,51], with asymmetric lineshapes to higher BE to account for Doniach-Šunjić broadening. The As 4*p* (peak 5) and O 2*p* (peak 6) states were each modeled as single peaks only because of the small energy difference between the $np_{3/2}$ and $np_{1/2}$ spin-orbit-split final states. (The O 2*p* peak appears smaller because of its much lower photoionization cross-section [52,53].) The As 4*s* states (peak 7) account for the isolated region at high BE. The relative intensity and peak positions of these Ni, As, and O states in CeNiAsO were constrained to have similar values as in LaNiAsO [11].

In principle, the fractional electron population for each state *i* depends on the integrated peak area I_i, corrected for the photoelectron cross-section σ_i and the inelastic mean free path (IMFP, λ_i). However, the IMFP can be neglected because it is the same for all photoelectrons, which travel through the same medium with similar kinetic energies. The fractional electron population then simplifies to [54]:

$$C_i = \frac{I_i/\sigma_i}{\sum_{j=1}^{n} I_i/\sigma_i}. \quad (2)$$

Multiplying C_i by the total number of valence electrons gives the electron population per formula unit for a given state. The O 2*s* states are located well below the Fermi edge and are assumed to be fully occupied [55,56]. The results of this fitting, applied to two separate samples and using two different sets of photoelectron cross-sections, are summarized in Table 3. The charge distribution obtained from this analysis, $[Ce^{2.9+}O^{2.0-}][Ni^{2.1+}As^{3.0-}]$, agrees well with the formal charge assignment based on the assumption of full electron transfer. The separate $[CeO]^{0.9+}$ and $[NiAs]^{0.9-}$ layers are then held together by ionic interactions, similar to conclusions reached from a Bader analysis on LaFePO [57].

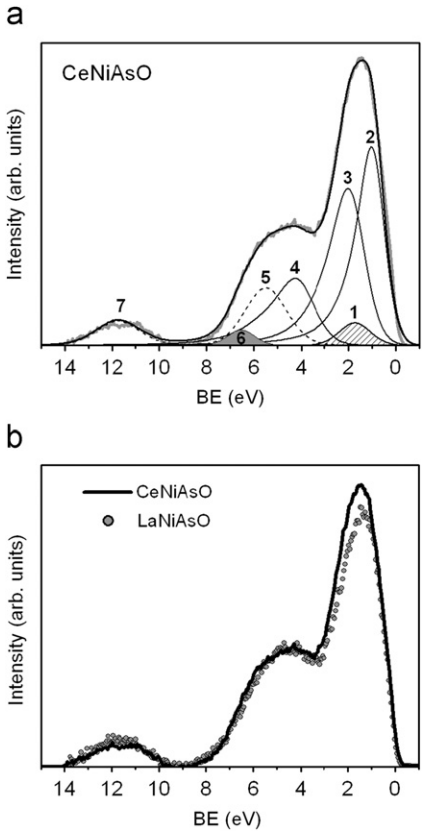

Fig. 8. (a) XPS valence band spectrum for CeNiAsO, fitted to component peaks as assigned in Table 3. (b) Valence band spectra for LaNiAsO and CeNiAsO, overlapped to highlight the location of Ce 4*f* states.

Table 3
Electron population (e^-) of valence states and charge distribution in CeNiAsO.

Atomic photoelectron cross-section, σ	Sample 1		Sample 2	
	Ref. [52][a]	Ref. [53][b]	Ref. [52][a]	Ref. [53][b]
Electron population				
Ce 4*f* (peak 1)	1.0	0.8	1.4	1.2
Ni 3*d* t_2 (peak 2)	3.4	3.1	3.5	3.2
Ni 3*d* *e* (peaks 3, 4)	4.9	4.5	4.8	4.3
As 4*p* (peak 5)	7.1	6.8	6.4	6.0
O 2*p* (peak 6)	5.7	6.2	5.8	6.2
As 4*s* (peak 7)	0.8	1.6	1.1	2.2
Total no. of e^-	23	23	23	23
Charge				
Ce	3.0+	3.2+	2.6+	2.8+
Ni	1.7+	2.4+	1.7+	2.5+
As	2.9−	3.4−	2.5−	3.2−
O	1.7−	2.2−	1.8−	2.2−
Average charges	$[Ce^{2.9+}O^{2.0-}][Ni^{2.1+}As^{3.0-}]$			

[a] Cross-section values, expressed relative to the C 1*s* cross-section of 13,600 barns, are: 0.06945 (Ce 4*f*), 0.19895 (Ni 3*d*), 0.06045 (As 4*p*), 0.1357 (As 4*s*), and 0.00965 (O 2*p*).

[b] Cross-section values, in units of megabarns, are: 0.0022 (Ce 4*f*), 0.0059 (Ni 3*d*), 0.0017 (As 4*p*), 0.0018 (As 4*s*), and 0.00024 (O 2*p*).

4. Conclusions

A comparison of the XPS and XANES spectra of the *RE*FeAsO (*RE*=La–Nd, Sm, Gd) and *RE*NiAsO (*RE*=La, Ce) series reveals minimal energy changes in the [*M*As] layer but substantial ones in the [*RE*O] layer as the *RE* component is varied. However, the shifts in the O 1*s* BEs do not arise from intraatomic effects involving a change in charge, but rather from interatomic effects reflecting the change in the Madelung potential as the *RE*–O distances are modified. The As 3*d* BEs in the *RE*FeAsO series and the Ni *L*-edge energy in the *RE*NiAsO series are insensitive to *RE* substitution, supporting the oft-made assertion that the [*RE*O] and [*M*As] layers can be treated independently. Although the As and O atoms are both found to be anionic, the shifts in the As 3*d* BEs are much less pronounced that those in the O 1*s* BEs, an indication of strong covalent character in the [*M*As] layer and strong ionic character in the [*RE*O] layer. The asymmetric lineshapes in the *M* 2*p* XPS spectra provide evidence for electronic delocalization within the [*M*As] layer. The presence of trivalent cerium is confirmed from the Ce 3*d* XPS and L_3-edge XANES spectra of CeFeAsO and CeNiAsO. Furthermore, a Ce 4*f* component can be detected in the valence band spectrum of CeNiAsO.

Acknowledgments

This work was supported through Discovery Grants to A.M. and R.G.C. from the Natural Sciences and Engineering Research Council (NSERC) of Canada. P.E.R.B thanks NSERC, Alberta Ingenuity, and the University of Alberta, for scholarship support. Access to the Kratos AXIS 165 XPS spectrometer was provided by the Alberta Centre for Surface Engineering and Science (ACSES), which was established with support from the Canada Foundation for Innovation (CFI) and Alberta Innovation and Science. The Ni *M*-edge XANES experiments were conducted at the CLS, which is supported by NSERC, NRC, CIHR, and the University of Saskatchewan. We thank Dr. Robert Gordon for assistance with the Ce L_3-edge XANES experiments at PNC/XOR-CAT facilities at the APS. The PNC/XOR facilities are supported by the US Department of Energy – Basic Energy Sciences, a major research support grant (MRS) from NSERC, the University of Washington, Simon Fraser University, and the APS. The APS is also supported by the US Department of Energy, Office of Science, Office of Basic Energy Sciences, under Contract DE-AC02-06CH11357.

Appendix A. Supplementary materials

Supplementary data associated with this article can be found in the online version at doi:10.1016/j.jssc.2010.04.010.

References

[1] H. Takahashi, K. Igawa, K. Arii, Y. Kamihara, M. Hirano, H. Hosono, Nature 453 (2008) 376–378.
[2] P. Quebe, L.J. Terbüchte, W. Jeitschko, J. Alloys Compd. 302 (2000) 70–74.
[3] Z. Li, G.F. Chen, J. Dong, G. Li, W.Z. Hu, D. Wu, S.K. Su, P. Zheng, T. Xiang, N.L. Wang, J.L. Luo, Phys. Rev. B 78 (2008) 060504-1–060504-4.
[4] G.F. Chen, Z. Li, D. Wu, G. Li, W.Z. Hu, J. Dong, P. Zheng, J.L. Luo, N.L. Wang, Phys. Rev. Lett. 100 (2008) 247002-1–247002-4.
[5] Z.A. Ren, J. Yang, W. Lu, W. Yi, G.C. Che, X.L. Dong, L.L. Sun, Z.X. Zhao, Mater. Res. Innov. 12 (2008) 105–106.
[6] Z.-A. Ren, J. Yang, W. Lu, W. Yi, X.-L. Shen, Z.-C. Li, G.-C. Che, X.-L. Dong, L.-L. Sun, F. Zhou, Z.-X. Zhao, Europhys. Lett. 82 (2008) 57002-1–57002-2.
[7] Y.-W. Ma, Z.-S. Gao, L. Wang, Y.-P. Qi, D.-L. Wang, X.-P. Zhang, Chin. Phys. Lett. 26 (2009) 037401-1–037401-4.
[8] P. Cheng, L. Fang, H. Yang, X.Y. Zhu, G. Mu, H.Q. Luo, Z.S. Wang, H.H. Wen, Sci. China Ser. G – Phys. Mech. Astron. G 51 (2008) 719–722.
[9] P.E.R. Blanchard, A.P. Grosvenor, R.G. Cavell, A. Mar, Chem. Mater. 20 (2008) 7081–7088.
[10] P.E.R. Blanchard, A.P. Grosvenor, R.G. Cavell, A. Mar, J. Mater. Chem. 19 (2009) 6015–6022.
[11] P.E.R. Blanchard, B.R. Slater, R.G. Cavell, A. Mar, A.P. Grosvenor, Solid State Sci. 12 (2009) 50–58.
[12] A.P. Grosvenor, R.G. Cavell, A. Mar, Struct. Bond. 133 (2009) 41–92.
[13] F. Bondino, E. Magnano, M. Malvestuto, F. Parmigiani, M.A. McGuire, A.S. Sefat, B.C. Sales, R. Jin, D. Mandrus, E.W. Plummer, D.J. Singh, N. Mannella, Phys. Rev. Lett. 101 (2008) 267001-1–267001-4.
[14] T. Kroll, S. Bonhommeau, T. Kachel, H.A. Dürr, J. Werner, G. Behr, A. Koitzsch, R. Hübel, S. Leger, R. Schönfelder, A.K. Ariffin, R. Manzke, F.M.F. de Groot, J. Fink, H. Eschrig, B. Büchner, M. Knupfer, Phys. Rev. B 78 (2008) 220502-1–220502-4.
[15] T. Kroll, F. Roth, A. Koitzsch, R. Kraus, D.R. Batchelor, J. Werner, G. Behr, B. Büchner, M. Knupfer, New J. Phys. 11 (2009) 025019-1–025019-11.
[16] E.Z. Kurmaev, R.G. Wilks, A. Moewes, N.A. Skorikov, Yu.A. Izyumov, L.D. Finkelstein, R.H. Li, X.H. Chen, Phys. Rev. B 78 (2008) 220503-1–220503-4.
[17] A. Koitzsch, D. Inosov, J. Fink, M. Knupfer, H. Eschrig, S.V. Borisenko, G. Behr, A. Köhler, J. Werner, B. Büchner, R. Follath, H.A. Dürr, arXiv: 0806.0833 (2008).
[18] A. Ignatov, C.L. Zhang, M. Vannucci, M. Croft, T.A. Tyson, D. Kwok, Z. Qin, S.-W. Cheong, arXiv: 0808.2134v2 (2008).
[19] Y. Zhang, Y.L. Chen, Y.J. Cui, C.H. Cheng, H. Zhang, Y. Zhao, Supercond. Sci. Technol. 22 (2009) 015007-1–015007-6.
[20] G.-F. Chen, Z. Li, D. Wu, J. Dong, G. Li, W.-Z. Hu, P. Zheng, J.-L. Luo, N.-L. Wang, Chin. Phys. Lett. 25 (2008) 2235–2238.
[21] B. Hunter, LHPM-Rietica, Version 1.7.7, International Union of Crystallography Commission on Powder Diffraction Newsletter, no. 20 (summer), 1998, ⟨www.rietica.org⟩.
[22] N. Fairley, CasaXPS, Version 2.3.9, Casa Software Ltd., Teighnmouth, Devon, UK, 2003, ⟨www.casaxps.com⟩.
[23] B. Ravel, M. Newville, J. Synchrotron Radiat. 12 (2005) 537–541.
[24] A.P. Grosvenor, R.G. Cavell, A. Mar, Chem. Mater. 18 (2006) 1650–1657.
[25] A.P. Grosvenor, R.G. Cavell, A. Mar, Phys. Rev. B 74 (2006) 125102-1–125102-10.
[26] A. Novosselov, E. Talik, A. Pajaczkowska, J. Alloys Compd. 351 (2003) 50–53.
[27] H. Berthou, C.K. Jørgensen, C. Bonnelle, Chem. Phys. Lett. 38 (1976) 199–206.
[28] J.C. Fuggle, M. Campagna, Z. Zolnierek, R. Lässer, A. Platau, Phys. Rev. Lett. 45 (1980) 1597–1600.
[29] J. Hormes, M. Pantelouris, G.B. Balazs, B. Rambabu, Solid State Ionics 136–137 (2000) 945–954.
[30] G. Kaindl, G. Schmiester, E.V. Sampathkumaran, P. Wachter, Phys. Rev. B 38 (1988) 10174–10177.
[31] Y. Jeon, F. Lu, H. Jhans, S.A. Shaheen, G. Liang, M. Croft, P.H. Ansari, K.V. Ramanujachary, E.A. Hayri, S.M. Fine, S. Li, X.H. Feng, M. Greenblatt, L.H. Greene, J.M. Tarascon, Phys. Rev. B 36 (1987) 3891–3894.
[32] T.L. Barr, Modern ESCA: the Principles and Practice of X-ray Photoelectron Spectroscopy, CRC Press, Boca Raton, FL, 1994.
[33] V. Dimitrov, T. Komatsu, J. Solid State Chem. 163 (2002) 100–112.
[34] A.P. Grosvenor, S.D. Wik, R.G. Cavell, A. Mar, Inorg. Chem. 44 (2005) 8988–8998.
[35] E.J. Little Jr., M.M. Jones, J. Chem. Educ. 37 (1960) 231–233.
[36] P.A.W. van der Heide, J. Electron Spectrosc. Relat. Phenom. 151 (2006) 79–91.
[37] Y. Uwamino, Y. Ishizuka, H. Yamatera, J. Electron Spectrosc. Relat. Phenom. 34 (1984) 67–78.
[38] S. Doniach, M. Šunjić, J. Phys. C: Solid State Phys. 3 (1970) 285–291.
[39] R.F. Egerton, M. Malac, J. Electron Spectrosc. Relat. Phenom. 143 (2005) 43–50.
[40] H.W. Nesbitt, D. Legrand, G.M. Bancroft, Phys. Chem. Miner. 27 (2000) 357–366.
[41] O. Karis, S. Svensson, J. Rusz, P.M. Oppeneer, M. Gorgoi, F. Schäfers, W. Braun, W. Eberhardt, N. Mårtensson, Phys. Rev. B 78 (2008) 233105-1–233105-3.
[42] S.K. Srivastava, A. Bahadur, J. Phys. Sci. 12 (2008) 201–206.
[43] C.D. Wagner, A.V. Naumkin, A. Kraut-Vass, J.W. Allison, C.J. Powell, J.R. Rumble Jr., NIST X-ray Photoelectron Spectroscopy Database, Version 3.5 (web version), National Institute of Standards and Technology, Gaithersburg, MD, 2003, ⟨srdata.nist.gov/xps⟩.
[44] A.P. Grosvenor, R.G. Cavell, A. Mar, R.I.R. Blyth, J. Solid State Chem. 180 (2007) 2670–2681.
[45] S. Ishibashi, K. Terakura, H. Hosono, J. Phys. Soc. Jpn. 77 (2008) 053709-1–053709-4.
[46] G. Xu, W. Ming, Y. Yao, X. Dai, S.-C. Zhang, Z. Fang, Europhys. Lett. 82 (2008) 67002-1–67002-5.
[47] T. Miyake, L. Pourovskii, V. Vildosola, S. Biermann, A. Georges, J. Phys. Soc. Jpn. 77 (2008) 99–102.
[48] I.A. Nekrasov, Z.V. Pchelkina, M.V. Sadovskii, JETP Lett. 87 (2008) 560–564.
[49] D.J. Singh, M.-H. Du, Phys. Rev. Lett. 100 (2008) 237003-1–237003-4.
[50] A.O. Shorikov, M.A. Korotin, S.V. Streltsov, D.M. Korotin, V.I. Anisimov, S.L. Skornyakov, arXiv:0804.3283v2 (2008).
[51] V.I. Anisimov, E.Z. Kurmaev, A. Moewes, I.A. Izyumov, Physica C 469 (2009) 442–447.
[52] J.H. Scofield, J. Electron Spectrosc. Relat. Phenom. 8 (1976) 129–137.
[53] J.J. Yeh, I. Lindau, At. Data Nucl. Data Tables 32 (1985) 1–155.
[54] J.F. Watts, J. Wolstenholme, An Introduction to Surface Analysis by XPS and AES, Wiley, Chichester, UK, 2003.
[55] V.V. Bannikov, I.R. Shein, A.L. Ivanovskii, arXiv:0810.2606 (2008).
[56] N. Chen, Y. Li, Open Condens. Matter Phys. J. 1 (2008) 13–18.
[57] S. Lebègue, Phys. Rev. B 75 (2007) 035110-1–035110-5.